Research Article

Maximized Ir atom utilization via downsizing active sites to single-atom scale for highly stable dry reforming of methane

Yangyang Li[1,2], Cun Liu[1,*] ID, Yang Su[1], Yang Zhao[3], Botao Qiao[1,*] ID

[1]CAS Key Laboratory of Science and Technology on Applied Catalysis, Dalian Institute of Chemical Physics, Chinese Academy of Sciences, Dalian 116023, Liaoning, China.
[2]University of Chinese Academy of Sciences, Beijing 100049, China.
[3]Dalian National Laboratory for Clean Energy, Dalian Institute of Chemical Physics, Chinese Academy of Sciences, Dalian 116023, Liaoning, China.

[*]**Correspondence to:** Prof. Botao Qiao, Dr. Cun Liu, CAS Key Laboratory of Science and Technology on Applied Catalysis, Dalian Institute of Chemical Physics, Chinese Academy Sciences, No. 457 Zhongshan Road, Dalian 116023, Liaoning, China. E-mail: bqiao@dicp.ac.cn; liucun@dicp.ac.cn

Abstract

Noble metals such as iridium with high Tammann temperature are inclined to sintering resistance and may be promising in the high-temperature dry reforming of methane (DRM) process, yet the low atom utilization remains intractable. Herein, we synthesized Ir/TiO_2 catalysts via the conventional incipient wetness impregnation method and further downsized the Ir species from a nanoparticulate to a single-atom scale by gradually decreasing Ir loadings from 1.0 wt.% to 0.01 wt.%. With the advantage of single atoms for maximized atom utilization, Ir single atoms were employed to enhance atom utilization in the DRM process. Various characterizations, such as aberration-corrected high-angle annular dark-field scanning transmission electron microscopy, CO adsorbed *in situ* diffuse reflectance infrared Fourier transform spectra and X-ray absorption spectra demonstrated the existence of Ir single atoms in 0.01% and 0.05% Ir/TiO_2. During the DRM process, Ir single-atom catalysts exhibited a better specific reaction rate of as high as 697.71 $mol_{CH4} \cdot g_{Ir}^{-1} \cdot h^{-1}$ at 750 °C compared with that over Ir nanoparticles of mere 447.12 $mol_{CH4} \cdot g_{Ir}^{-1} \cdot h^{-1}$, which unambiguously showed the remarkable Ir atom utilization over Ir single atoms. Besides, the Ir single-atom catalysts also exhibited excellent stability during the DRM process for 50 h and revealed outstanding anti-coking and good sintering-resistance properties examined by the thermal gravimetric analysis-mass spectrometer and Raman spectroscopy. The strategy of employing Ir single atoms for the maximum atom

utilization in the high-temperature reaction process can pave the way for better exploitation of noble metals in other industrial reaction processes.

INTRODUCTION

Carbon dioxide and methane are major parts of greenhouse gases, which are notoriously responsible for the year-on-year global warming and unfavorable climate change[1-4]. Therefore, to retard or even reverse those unsettling environmental issues, greenhouse gases should be scientifically stored[5,6] or converted into value-added chemicals[7-9]. To this end, dry reforming of methane (DRM) process, during which carbon dioxide and methane are simultaneously converted into a mixture of monoxide and hydrogen, known as syngas for the industrially downstream hydroformylation[10], carbonylation[11], and Fischer-Tropsch processes[12-14], is widely investigated in both academic and industrial fields[15]. Therein, one main research point is the selection of active metals. Generally, transition metals, especially Ni-based catalysts[2,16-18] and noble metals (Rh[19], Ru[20], Pt[21], Pd[22], Ir) are both hotspots for the DRM process. Although transition metals have abundant reserves on Earth and show high catalytic activity during the DRM process, they also severely suffer from sintering and the consequent carbon deposition at high temperatures[23], which inevitably causes high operational costs for coke elimination of facilities and regeneration of catalysts. Alternatively, noble metals with excellent activity and stability are promising candidates for the DRM process. Meanwhile, their long-term anti-coking properties[24,25] can efficiently prevent the shutdown of facilities and profitably offset the expense of noble metals in return.

Compared with the other noble metals suitable for the DRM process, iridium has the highest Tammann temperature[13,26], probably inferring the best thermal stability even at harsh reaction conditions. Overall, iridium species have been mainly investigated as either promoters or active sites in the DRM process. As for iridium species as promotors, especially over dual Ni-Ir systems[27-30], iridium species can efficiently transform the carbon depositions generated from CH_4 activation over the adjacent Ni nanoparticles and the carbonate species formed from CO_2 adsorbed on the support into monoxide, thus fostering the elimination of carbon depositions and consequently rendering the improvement of long-term stability. However, with regard to iridium species as active sites, few researches focus on the correlation of intrinsic properties of iridium with catalytic performances while most reports primarily pay attention to how the physiochemical properties of supports, for example, oxygen vacancies[31], acidity[32] and metal-support interaction[33], affect the CO_2 activation and stability during DRM process. Considering the scarcity of iridium, the intrinsic properties of Ir atoms should be exploited as far as possible to maximize atom utilization.

Single-atom catalysts (SACs) have gained extensive spotlights in the heterogeneous catalysis field due to their outstanding catalytic activity and maximized metal atom utilization efficiency[34-40]. For example, Zhou *et al.* have synthesized Ru single atoms supported on nitrogen-doped carbon (Ru_1/NC) which were applied in the high-temperature propane dehydrogenation[41]. Compared with the Ru nanoparticulate counterparts, the specific rate of the production of propylene per metal sites increased as the size of the Ru particle decreased and peaked at 428 $mol_{C3H6} \cdot g_{Ru}^{-1} \cdot h^{-1}$ over Ru_1/NC. In addition, Han *et al.* have constructed Rh single atoms supported on CeO_2 (Rh_1/CeO_2) for the low-temperature CO oxidation, during which Rh_1/CeO_2 attained a specific rate of 14.3 $mol_{CO} \cdot h^{-1} \cdot g_{Rh}^{-1}$ while only 3.1 $mol_{CO} \cdot h^{-1} \cdot g_{Rh}^{-1}$ was yielded over Rh nanoparticles[42]. The abovementioned reports undoubtedly demonstrate the effectiveness of SACs on maximized atom utilization. Therefore, it is plausible that Ir atom utilization may also be greatly improved via the strategy of downsizing Ir active sites to a single-atom scale since our group has previously revealed an excellent specific reaction rate over Ni SACs in the DRM process[43,44].

Herein, we supported Ir species on TiO_2 via the conventional incipient wetness impregnation method and acquired Ir nanoparticles, atomically dispersed Ir and Ir SACs by gradually scaling down the Ir loading from 1.0 wt.% to 0.01 wt.%. Combining various characterizations, it was evidenced that Ir SACs were successfully supported on TiO_2 and meanwhile had stronger electronic interaction with TiO_2 compared with that with bulk Ir nanoparticles. Therefore, Ir SACs showed a better specific reaction rate of 697.71 $mol_{CH4} \cdot g_{Ir}^{-1} \cdot h^{-1}$ at 750 °C in the DRM process than that of 447.12 $mol_{CH4} \cdot g_{Ir}^{-1} \cdot h^{-1}$ over Ir nanoparticles. Besides, the as-synthesized Ir SACs also exhibited decent stability resulting from the anti-coking properties of Ir species, which further sheds light on the rational design of prospectively stable Ir single-atom DRM catalysts with maximum atom utilization.

EXPERIMENTAL

Synthesis of iridium SACs and nanoparticles supported on TiO_2

The conventional incipient wetness impregnation method was employed to prepare Ir SACs and nanoparticles supported on TiO_2. In detail, 0.02, 0.10, 0.41, 1.02, and 2.04 mL H_2IrCl_6 (purchased from Energy Chemical, 98%) aqueous solution (4.9 mg_{Ir}/mL) were added into 50 mL deionized water for 0.01 wt.%, 0.05 wt.%, 0.2 wt.%, 0.5 wt.%, and 1.0 wt.% Ir/TiO_2, respectively, and then 1.0 g commercial TiO_2 (rutile phase, purchased from Aladdin, 99%) was added and continuously stirred for 1 h. Afterwards, this solution was evaporated at 70 °C in a water bath under stirring conditions. The as-obtained solid was dried at 80 °C for 12 h and calcined at 500 °C for 4 h. The low loading (0.01 wt.% and 0.05 wt.%) and high loading (0.2 wt.%, 0.5 wt.%, and 1.0 wt.%) of Ir/TiO_2 catalysts were denoted as x% Ir/TiO_2, respectively, where x represents the nominal metal loading of iridium. The reproducibility was also well confirmed by preparing three batches of catalysts for DRM tests, during which similar catalytic results were observed [Supplementary Figure 1].

Characterizations

The actual Ir loadings of x% Ir/TiO_2 catalysts were determined by an inductively coupled plasma optical emission spectrometer (ICP-OES) on an ICPS-8100 instrument (Shimadzu Co., Ltd.). Textural properties were measured by N_2 adsorption-desorption isotherms recorded at 77 K using Quantachrome station. Specific surface areas were calculated from the adsorption branch using the Brunauer-Emmett-Teller (BET) method. X-ray diffraction (XRD) patterns were recorded with a PW3040/60 X'Pert PRO PANalytical diffractometer with Cu Kα radiation (λ = 0.15432 nm) operating at 40 kV and 40 mA in the range of 2θ = 10°-80°.

Temperature-programmed reduction (H_2-TPR) was performed on a Micromeritics AutoChem II 2920 instrument. For each experiment, 100 mg of each sample was placed in a quartz reactor and pretreated in flowing Ar (30 $mL \cdot min^{-1}$) at 300 °C for 30 min to remove the physically adsorbed water. After cooling to 30 °C, the temperature was gradually increased to 800 °C with a ramp of 10 $°C \cdot min^{-1}$ under a flow of 10 vol.% H_2/Ar (30 $mL \cdot min^{-1}$), and the thermal conductivity detector (TCD) then monitored the H_2 consumption. The CH_4-temperature-programmed surface reaction (TPSR) experiments were also performed using the same instrument. Typically, 50 mg of sample was placed in a quartz reactor and reduced with 10% vol.% H_2/Ar (30 $mL \cdot min^{-1}$) for 1 h at 500 °C. After purging with Ar and cooling down to room temperature, the gas was switched to 1 vol.% CH_4/He, and the catalyst was gradually heated to 800 °C at a ramping rate of 10 $°C \cdot min^{-1}$ with a flow rate of 30 $mL \cdot min^{-1}$. Reaction products were analyzed online using a mass spectrometer (MS) (GSD350 OmniStar).

The high-angle annular dark-field scanning transmission electron microscopy (HAADF-STEM) images were conducted on JEOL JEM-2100F operating at an accelerating voltage of 200 kV. The aberration-

corrected HAADF-STEM (AC-HAADF-STEM) images were obtained on JEOL JEM-ARM200F operated at 200 kV equipped with a Gatan Quantum 965 image filter system. Before the measurement, the samples were ultrasonically dispersed in ethanol and deposited onto carbon films.

In situ X-ray photoelectron spectroscopy (XPS) analysis was performed using a ThermoFischer ESCALAB 250Xi instrument equipped with an Al Kα excitation source (1,486.8 eV). Adventitious carbon was employed as the internal standard (C 1s = 284.8 eV). Before the measurement, the as-synthesized samples underwent *in situ* reduction in 10 vol.% H_2/N_2 at 500 °C for 1 h in an ultra-high vacuum (UHV)-connected high-pressure gas chamber. After this pre-treatment, the samples were transferred into the analyzer chamber under UHV conditions.

In situ diffuse reflectance infrared Fourier transform spectra (DRIFTs) of adsorbed CO were collected on an infrared spectrometer (Vertex 70, Bruker) equipped with a liquid nitrogen-cooled mercury cadmium telluride (MCT) detector. Spectra were collected in the range 1,000-4,000 cm^{-1} range at a resolution of 4 cm^{-1}, averaging 32 scans. Prior to the analysis, the sample was reduced *in situ* within the reaction cell under a flow of 10 vol.% H_2/He (30 mL·min^{-1}) at 500 °C for 1 h. The background spectrum was recorded after purging with He for 30 min to cool the chamber to room temperature. Subsequently, 5 vol.% CO/He was introduced into the reaction cell, and the spectra were collected until no further changes were observed. Finally, pure He was introduced to remove the gaseous CO, and additional spectra were recorded.

Thermogravimetric analysis (TGA) was performed using a Simultaneous Thermal Analyzer (STA449F5). The catalysts were initially heated to 200 °C in Ar flow with a ramp rate of 5 °C·min^{-1} and maintained at the temperature for 0.5 h to remove physically adsorbed water. Subsequently, the samples were further heated to 800 °C following the same heating protocol. Raman spectroscopy was conducted using a combined atomic force microscopy (AFM)-Raman system (Bruker NanoWizard Ultra Speed & inVia Raman) with a 532 nm excitation laser.

The X-ray absorption spectra (XAS), including X-ray absorption near-edge structure (XANES) and extended X-ray absorption fine structure (EXAFS) at Ir *L*-edge analysis was performed with Si (111) crystal monochromators at the BL14W1 beamlines at the Shanghai Synchrotron Radiation Facility (SSRF) (Shanghai, China). Before the analysis at the beamline, samples were pressed into thin sheets 1 cm in diameter and sealed using Kapton tape film. The XAFS spectra were recorded at room temperature using a 4-channel Silicon Drift Detector (SDD) Bruker 5040. Ir *L*-edge EXAFS spectra were recorded in fluorescence mode. Negligible changes in the line shape and peak position of Ir *L*-edge XANES spectra were observed between two scans taken for a specific sample. The XAFS spectra of these standard samples (Ir, IrO_2) were recorded in transmission mode for 0.05% Ir/TiO_2, and a solid detector was used to achieve high data quality. For the XAS spectra of reduced catalysts, the samples were reduced in a fixed-bed reactor with 10 vol% H_2/Ar at 500 °C. The spectra were processed and analyzed using the Athena and Artemis software code.

Catalytic tests

Methane dry reforming reaction over different samples was evaluated at atmospheric pressure in a fixed bed quartz reactor (inner diameter = 0.76 cm) with 50 mg catalysts. Before each catalytic test, the sample was *in situ* reduced at 500 °C for 60 min under 10 vol.% H_2/Ar and then purged for 30 min with Ar until the temperature increased to 750 °C. The mixture gas of CH_4 and CO_2 (20 vol.% CH_4, 20 vol.% CO_2, 1 vol.% N_2, Ar balanced) with a total flow rate of 32.3 mL/min [gas hourly space velocity (GHSV) of 38,760 mL·g_{cat}^{-1}·h^{-1}] was fed into the fixed bed reactor. The specific reaction rate and turnover frequency (TOF) for CH_4 and

CO_2 conversion were measured at much higher GHSV (using 2-50 mg of catalyst diluted by 70-80 mesh quartz sand, wherein the CH_4 and CO_2 conversions were controlled below 25%). The reactor temperature was recorded with a thermocouple inserted close to the catalytic bed of the reactor. The reactants and products were analyzed by a gas chromatograph equipped with a thermal conductivity detector and a TDX-01 column connected online with the Ar as the gas carrier. N_2 in the feed stream was employed as an internal standard to compensate for the changes in the concentration due to volume expansion after DRM reaction. The CO_2 and CH_4 conversions were determined according to:

$$\delta = \frac{[N_2]_{out}}{[N_2]_{in}}$$

$$C_{CH_4(out)} = \frac{[CH_4]_{out}}{\delta}, \ C_{CH_4(in)} = [CH_4]_{in}$$

$$C_{CO_2(out)} = \frac{[CO_2]_{out}}{\delta}, \ C_{CO_2(in)} = [CO_2]_{in}$$

$$C_{H_2(out)} = \frac{[H_2]_{out}}{\delta}, \ C_{CO(out)} = \frac{[CO]_{out}}{\delta}$$

$$X_{CH_4} = \frac{C_{CH_4(in)} - C_{CH_4(out)}}{C_{CH_4(in)}}$$

$$X_{CO_2} = \frac{C_{CO_2(in)} - C_{CO_2(out)}}{C_{CO_2(in)}}$$

$$H_2/CO = \frac{C_{H_2(out)}}{C_{CO(out)}}, \ C_{H_2(out)} = [H_2]_{out}, \ C_{CO(out)} = [CO]_{out}$$

$$Carbon \ balance = \frac{C_{CO(out)} + C_{CO_2(out)} + C_{CH_4(out)}}{C_{CO_2(in)} + C_{CH_4(in)}}$$

where $[CH_4]$ and $[CO_2]$ denoted the concentrations (vol.%) detected by gas chromatography (GC), while C_{CH4} and C_{CO_2} indicated the actual concentration after calibrations. Methane and CO_2 specific reaction rate $(mol \cdot g_{Ir}^{-1} \cdot h^{-1})$ were calculated according to:

$$Rate \ CH_4 = \frac{(F_t * [CH_4]_{in} * X_{CH_4})}{(Weight \ of \ catalyst \times \ w_{Ir} \times 22.4 \times 10^3)} \times 60$$

$$Rate \ CO_2 = \frac{(F_t * [CO_2]_{in} * X_{CO_2})}{(Weight \ of \ catalyst \times \ w_{Ir} \times 22.4 \times 10^3)} \times 60$$

where F_t represents the total flow $(mL \cdot min^{-1})$, whereas ω_{Ir} is the iridium metal loading (wt%). TOF (s^{-1}), defined as the number of CH_4 or CO_2 molecules converted per exposed catalytic site per second, is determined based on:

$$TOF = \frac{(F_t * [CH_4]_{in} * X_{CH_4})}{Weight\ of\ catalyst \times \frac{w_{Ir}}{192.22} \times Dispersion \times 22.4 \times 10^3 \times 60}$$

$$Dispersion = \frac{1.1053}{d_{VA}}$$

where the mean particle size (d_{VA}) is obtained from STEM images[45,46], specifically by selecting more than ten images and measuring over one hundred particles. The derivation process of the dispersion formula is presented in the Supplementary Materials. As for Ir single atom/atomically dispersed Ir species, all the Ir atoms are directly bonded with TiO_2 support and exposed to the catalytic environment, thus showing 100% dispersion[47,48].

Before carrying out the kinetic experiment, it is necessary to eliminate external diffusion by changing the linear velocity. It is worth mentioning that the CH_4 conversion is almost the same when the liner velocity is above 7.89 cm/min [Supplementary Table 1 and Supplementary Figure 2], at which the external diffusion on the reaction is experimentally eliminated.

RESULTS AND DISCUSSION

Iridium species were dispersed onto the rutile TiO_2 support via the conventional incipient wetness impregnation method with H_2IrCl_6 as the precursor. In order to downsize the Ir species from a nanoparticulate scale to an atomically dispersed or even single-atom scale, the nominal Ir loading was gradually decreased from 1.0 wt.% to 0.01 wt.%. The as-obtained samples were denoted as x% Ir/TiO_2, where x represented the nominal iridium loading. As shown in Figure 1A, XRD patterns of all the samples exhibit the retention of the rutile phase, while the absence of both iridium and IrO_2 can be attributed to the low loading and/or high dispersion of Ir species on TiO_2 support. The N_2 adsorption-desorption isotherms of the above samples [Figure 1B] also bear few differences and the corresponding BET surface areas [Supplementary Table 2] of around 40 m^2/g nearly remain unchanged. The actual Ir loadings of x% Ir/TiO_2 samples detected by ICP-OES range from 0.0057 wt.% to 0.7888 wt.% [Supplementary Table 2], which unambiguously demonstrates that the successful deposition of Ir species on TiO_2 does not have any impact on the physical structure of supports.

The distributions of Ir species were directly observed via the AC-HAADF-STEM. As can be seen in Figure 2A and B, Ir single atoms or atomically dispersed Ir species can be attained when we lower the Ir loadings below 0.05 %. Further examining AC-HAADF-STEM images with a lower magnitude of 0.05% Ir/TiO_2 [Supplementary Figure 3] also testifies to high dispersion of Ir single atoms. It is worth noting that a calcination temperature of 500 °C is the prerequisite for acquiring highly dispersed Ir single atoms as a higher calcination temperature, such as 750 °C, leads to Ir agglomeration [Supplementary Figures 4 and 17]. As for the samples with Ir loadings of 0.2%-1.0% [Figure 2C-E], Ir species are mainly in the form of nanoparticles with a similar average size of 1.78 nm regardless of increasing Ir loadings. As mentioned above, the resistance of Ir sintering can result from the inherently high Tammann temperature, which is a promising merit for giving excellent stability at harsh temperatures in the DRM process.

To further estimate the dispersion and chemical properties of Ir species on Ir/TiO_2 catalysts, CO was used as a probe in the *in situ* diffuse reflectance infrared Fourier transform (DRIFT) spectra to get a structural comparison after *in situ* reducing the samples at 500 °C. In a typical experiment, after CO reached saturation adsorption, pure He was purged into the reaction chamber to remove the physically adsorbed CO
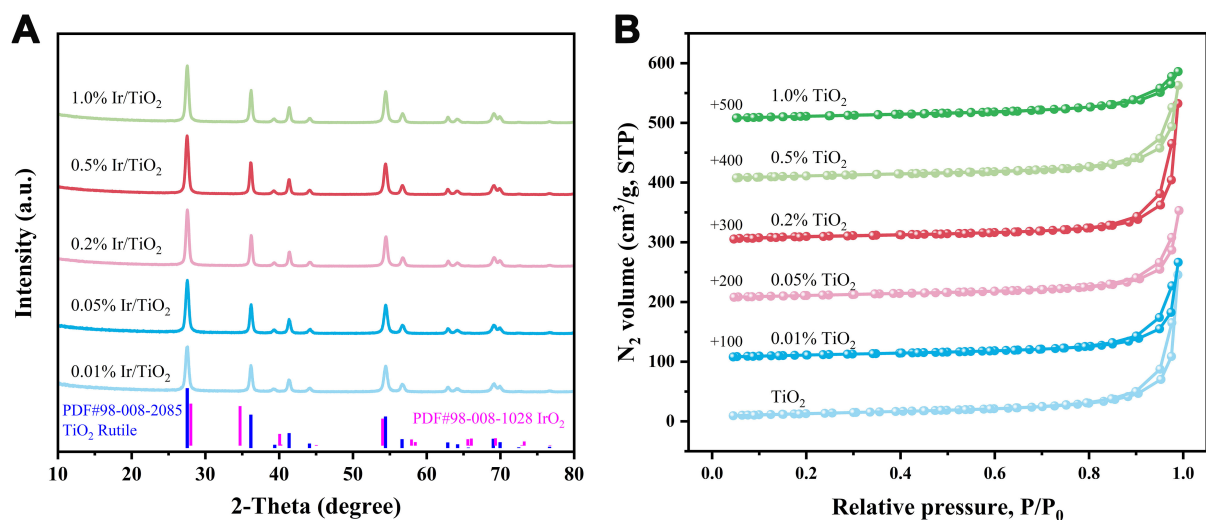
Figure 1. Physical properties of different Ir/TiO$_2$ samples. (A) XRD patterns and (B) N$_2$ adsorption-desorption isotherms. XRD: X-ray diffraction.
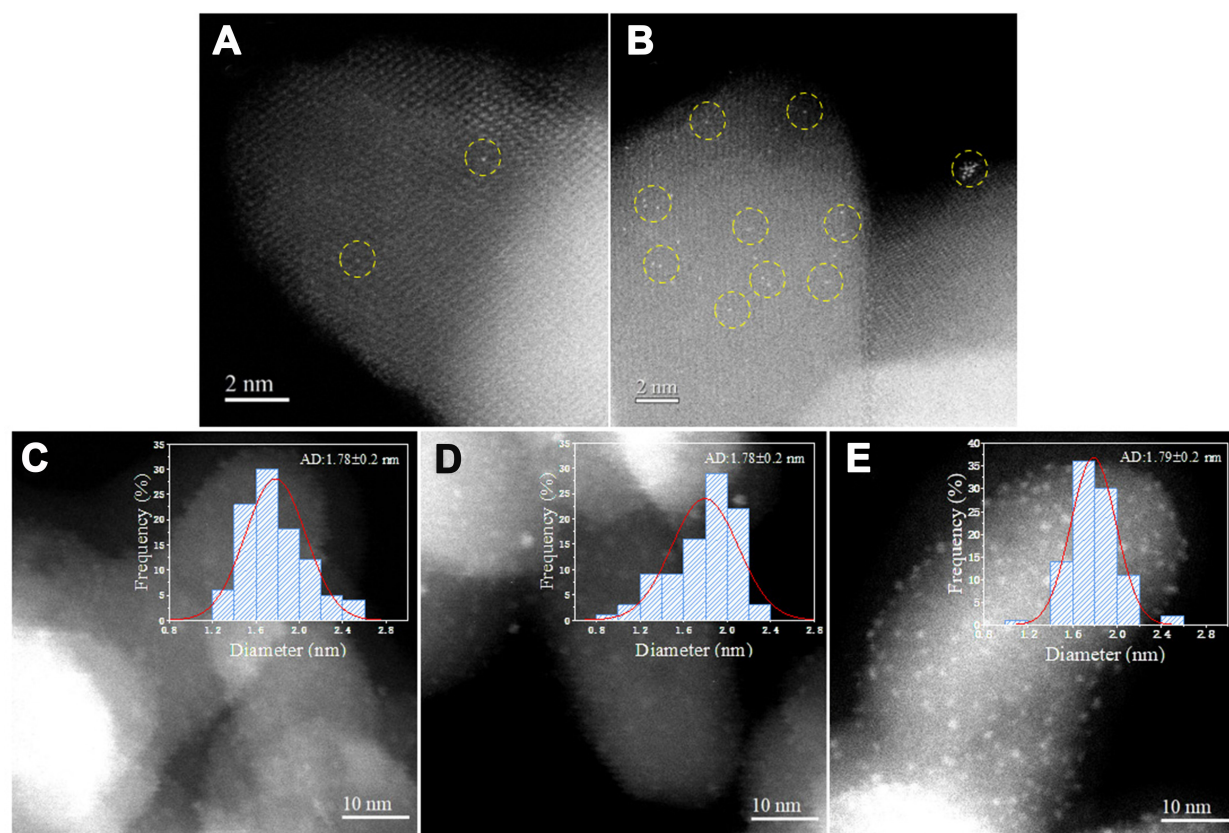

Figure 2. AC-HAADF-STEM images of (A) 0.01% Ir/TiO$_2$; (B) 0.05% Ir/TiO$_2$ and HAADF-STEM images of (C) 0.2% Ir/TiO$_2$; (D) 0.5% Ir/TiO$_2$; (E) 1.0% Ir/TiO$_2$ samples after reduction at 500 °C. AC-HAADF-STEM: Aberration-corrected high-angle annular dark-field scanning transmission electron microscopy.

while the chemically adsorbed CO remained on the metal sites. Typically, four characteristic adsorption peaks can be observed in the CO-DRIFT spectra of Ir species. The two features at 2,058 and 1,990 cm^{-1} can be assigned to the dicarbonyl Ir$^+$(CO)$_2$ species, which signals the existence of Ir single atoms, similar to the
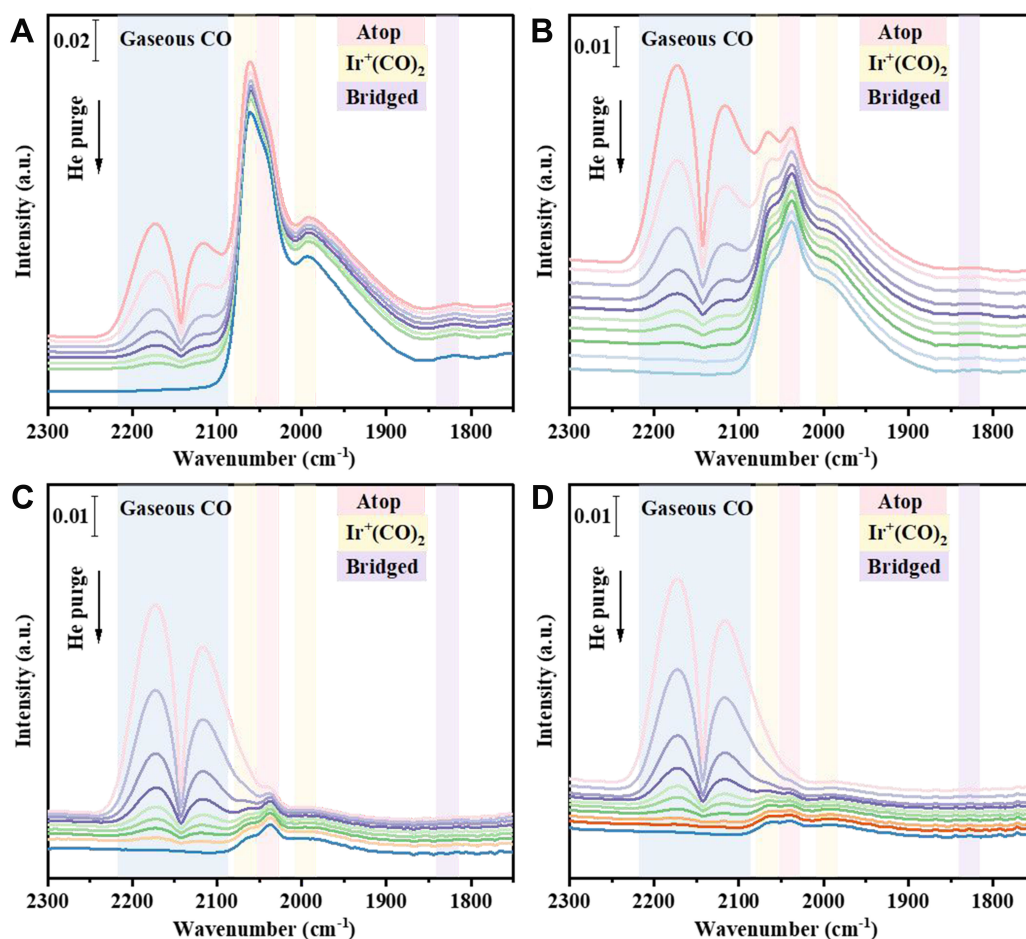
Figure 3. DRIFT spectra of CO adsorption on Ir/TiO_2 with different Ir loadings after in-situ reduction at 500 °C. (A) 1.0% Ir/TiO_2; (B) 0.5% Ir/TiO_2; (C) 0.2% Ir/TiO_2; (D) 0.05% Ir/TiO_2. DRIFT: Diffuse reflectance infrared Fourier transform spectra.

results of peaks at around 2,065 and 1,985 cm^{-1} reported by Lu *et al.*[49] and Jin *et al.*[50]. In addition, the peak at 2,036 cm^{-1} is attributed to the atop binding of CO on Ir nanoclusters while the broad peak centered at 1,820 cm^{-1} is ascribed to bridged CO species, which are the indicators of Ir clusters or nanoparticles[45,49,50]. For 1.0%, 0.5% and 0.2% Ir/TiO_2 samples [Figure 3A-C], all the abovementioned four CO adsorbed peaks can be clearly identified, suggesting that Ir species have relatively wide distributions in those samples. As for 0.05% Ir/TiO_2 [Figure 3D], two main dicarbonyl and one weak atop CO adsorption peaks can be ascertained. Combined with the devoid of bridged CO species, it is rational that Ir species are atomically dispersed on TiO_2, which is in accordance with the results obtained from the AC-HAADF-STEM images. Although the low Ir loading of 0.01% Ir/TiO_2 sets obstacles for evidently monitoring the adsorption peaks [Supplementary Figure 5], barely can any atop and bridged adsorption peaks be detected even after enlarging the specific spectra [Supplementary Figure 6], thus consolidating the Ir single-atom state in 0.01% Ir/TiO_2.

Furthermore, after downsizing the Ir species from the nanoparticulate to single-atom scale, the interaction between Ir species and TiO_2 support can be switched into a stronger state due to the direct contact between Ir single atoms and oxygen atoms of the TiO_2 support. In order to give evidence of this inference, XPS experiments were conducted after *in situ* reducing the Ir/TiO_2 samples at 500 °C. As illustrated in Figure 4A, the binding energy of Ir $4d_{5/2}$ peak gradually increases from 296.64 eV of 1.0% Ir/TiO_2 to 298.11 eV of 0.05%
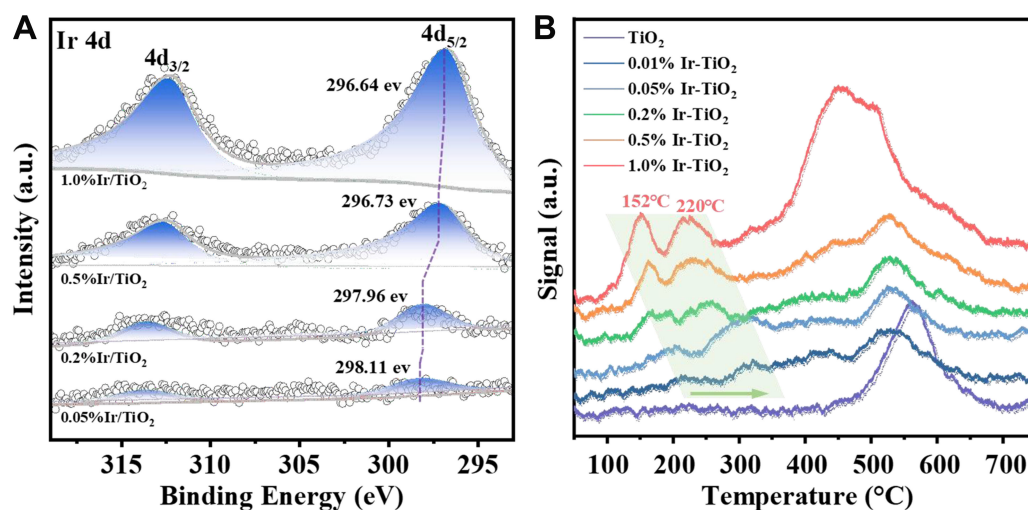
Figure 4. Interactions between Ir species and TiO$_2$ support of different samples. (A) *In situ* Ir 4d XPS spectra and (B) H$_2$-TPR profiles. XPS: X-ray photoelectron spectroscopy; TPR: temperature-programmed reduction.
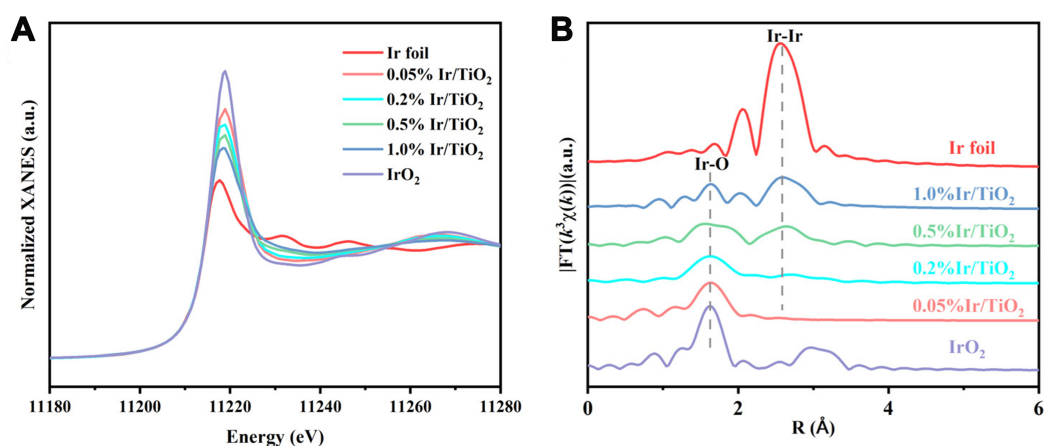

Figure 5. (A) Ir L_3 XANES spectra and (B) Fourier-transformed k^3-weighted EXAFS spectra of Ir foil, IrO$_2$, and different Ir/TiO$_2$ samples. XANES: X-ray absorption near-edge structure; EXAFS: extended X-ray absorption fine structure.

Ir/TiO$_2$, indicating that exposing only Ir single atoms can forge stronger interaction between Ir species and lattice oxygen of TiO$_2$. Moreover, the reduction peaks at 152 and 220 °C attributed to the reduction of Ir species in the H$_2$-TPR profiles [Figure 4B] also shift to higher temperatures after downsizing the scale of Ir species. This resistance to reduction is also an accompanying benefit of Ir single atoms anchored on TiO$_2$, which may be conducive to enhancing stability in the DRM process. Moreover, the reduction peaks of TiO$_2$ supports also shift to lower temperatures due to the occurrence of hydrogen spillover compared with the bare TiO$_2$ support.

X-ray absorption spectroscopy was carried out on different Ir/TiO$_2$ samples to further gain insight into the local coordination state of Ir atoms. The Ir L_3-edge XANES spectroscopy [Figure 5A] shows the white lines of Ir/TiO$_2$ samples between Ir and IrO$_2$, which reveal the partially positive state of Ir species consistent with the *in situ* XPS results. In addition, the Fourier-transformed (FT) k^3-weighted EXAFS profiles were obtained to further study the fine structure and local environment of Ir species [Figure 5B]. As for the 0.05%Ir/TiO$_2$, the Ir-O scattering at ~2.03 Å is exclusively detected and no Ir-Ir scattering can be observed, thus

confirming the single-atom Ir species supported on TiO_2. However, for 0.2%, 0.5% and 1.0% Ir/TiO_2 samples, the Ir-Ir scattering at 2.73 Å is gradually intensified with the average coordination number of Ir-Ir scattering path increasing to 1.35, 2, 2.79, respectively [Supplementary Table 3]. Therefore, combined with the AC-HAADF-STEM, *in situ* CO DRIFTs and EXAFS results, we can unambiguously confirm that the Ir species of 0.01% Ir/TiO_2 and 0.05% Ir/TiO_2 samples are in single-atom state, while those of 0.2%-1.0% Ir/TiO_2 samples are mainly composed of nanoparticles.

DRM is a highly endothermic reaction that often requires a high temperature. Prior experiments have shown the ideal reaction temperature of 650 to 800 °C, especially higher than 750 °C, to effectively activate both CH_4 and CO_2 molecules [Supplementary Figure 7]. However, the subsequent sintering of active sites forming thermodynamical stable agglomerates is detrimental to the catalytic stability due to either a decrease in active metal sites and/or the concomitant formation of coke depositions. Considering the expense of noble metals such as iridium, the maximum utilization of Ir atoms while maintaining catalytic stability is of great importance. To cater to those criteria, Ir loading was decreased to scale down the Ir species from a nanoparticulate to a single-atom scale, and the corresponding DRM performances for 50 h are shown in Figure 6. During the DRM process over different Ir/TiO_2 samples, CO_2 conversion [Figure 6B] is constantly higher than CH_4 conversion [Figure 6A] due to the concomitant occurrence of the reverse water-gas shift reaction. However, with increasing Ir loading, both CH_4 and CO_2 conversions rise along with the gradually growing H_2/CO ratio [Figure 6C], which unequivocally indicates the progressive dominance of the DRM process in the whole reaction[8,51]. Other than CO and H_2, water is the only detected by-product due to the simultaneous reverse water-gas shift reaction. During the time-on-stream of 50 h, all the Ir catalysts display excellent stability, which agrees well with our experimental strategy of selecting Ir species with high Tammann temperature as the stable active sites for DRM even at a high temperature of 750 °C. Besides, it is worthwhile to mention that although the CH_4 conversions over Ir nanoparticles are higher than that over atomically dispersed Ir or Ir single atoms, increasing the Ir loading from, for example, 0.05% to 0.2%, the CH_4 conversion is not proportionally increased, which implies the effective atom utilization over Ir SACs compared with the nanoparticulate counterparts. This reasonable speculation is further tested by purposedly controlling the CH_4 conversion below 25% to quantitatively compare the TOF values and specific reaction rates over different Ir/TiO_2 catalysts[43,52]. As listed in Table 1 and Supplementary Table 4, considering the exposed Ir atoms as active sites, the TOF values over Ir nanoparticles are slightly higher than that over Ir single atoms, which can be attributed to the existence of step, corner and kink sites on nanoparticles for better activation of reactants. Nevertheless, when all the Ir atoms are considered to acquire specific reaction rates for the assessment of atom utilization, on the contrary, the specific reaction rates over Ir single atoms are higher than those over Ir nanoparticles because of the fully exposing Ir atoms to the reactant molecules[47,48,53]. Particularly, the specific reaction rate over 0.05% Ir/TiO_2 is as high as 697.71 $mol_{CH4} \cdot g_{Ir}^{-1} \cdot h^{-1}$ at 750 °C while that only ranges from 447.12 to 499.32 $mol_{CH4} \cdot g_{Ir}^{-1} \cdot h^{-1}$ over Ir nanoparticles, which corroborates the highest Ir atom utilization from the economic perspective after downsizing the Ir species to single-atom scale while part of the atoms inside Ir nanoparticles do not participate in the catalytic process. Besides, we also compare the DRM performance over 0.05% Ir/TiO_2 with reported results over transition and noble metals, which demonstrate the excellent coke-resistance and higher specific reaction rate over the single-atom scale Ir species [Supplementary Table 5]. Other Ir SACs supported on, such as SiO_2, MgO and Al_2O_3, were also tested in the DRM process. The results show that 0.05% Ir/SiO_2, 0.05% Ir/MgO and 0.05% Ir/Al_2O_3 suffer from either low activity or poor stability [Supplementary Figures 8-11]. Therefore, TiO_2, as a reducible support with abundant oxygen vacancies, can provide more sites to stabilize single atoms for the improved catalytic activity and stability in DRM process.

Table 1. Catalytic reaction rate during DRM process over different loadings of Ir catalysts

| Sample | Dispersion (%) | TOF (s^{-1})[a] | | Specific reaction rate[a] ($mol \cdot g_{Ir}^{-1} \cdot h^{-1}$) | | Temperature (°C) |
		CH_4	CO_2	CH_4	CO_2	
0.01% Ir/TiO_2	100	12.02	20.05	225.09	375.52	700
		32.07	60.99	600.56	1,142.22	750
0.05% Ir/TiO_2	100	10.40	17.29	194.86	323.83	700
		37.25	68.55	697.71	1,283.78	750
0.2% Ir/TiO_2	62.10	17.28	28.38	200.99	330.07	700
		42.93	72.10	499.32	838.52	750
0.5% Ir/TiO_2	61.82	17.80	27.93	206.05	323.41	700
		39.60	60.28	458.49	697.87	750
1.0% Ir/TiO_2	61.47	14.58	22.19	167.80	255.43	700
		38.84	56.26	447.12	647.71	750

[a]In the kinetic activity assessment, equilibrium conversion was determined based on triplicate evaluations [Supplementary Table 4 and Supplementary Figure 18]. The reaction gas mixture consisted of CH_4 and CO_2 (20 vol.% CH_4, 20 vol.% CO_2, 1 vol.% N_2, balance Ar). DRM: Dry reforming of methane; TOF: turnover frequency.
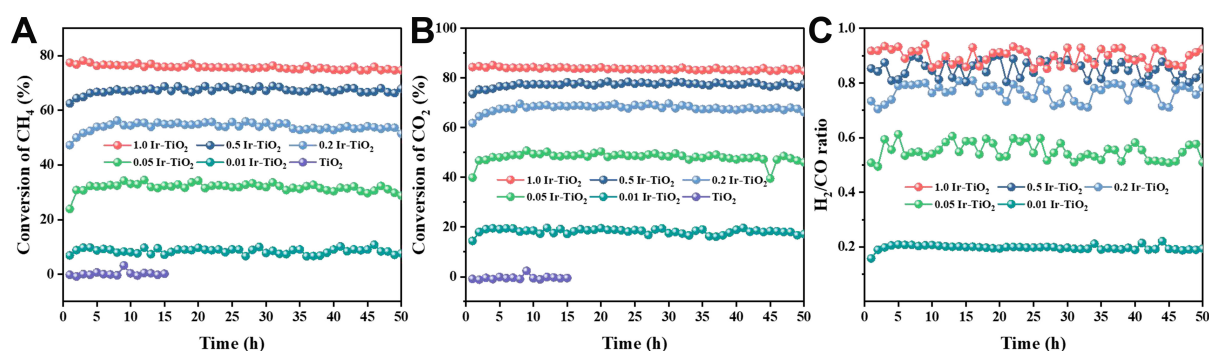

Figure 6. DRM performances over different loadings of Ir/TiO_2 catalysts. (A) CH_4 conversion (B) CO_2 conversion and (C) the ratio of H_2/CO. DRM: Dry reforming of methane.

The ability to activate CH_4 and the corresponding cracking mechanism were investigated via TPSR experiments using diluted CH_4 as the sole reactant because CH_4 cracking is of great significance during the DRM process. In CH_4-TPSR experiments, two consecutive processes are involved: the CH_4 decomposition ($CH_4 \rightarrow C + 2H_2$) and the formation of CO ($C + O^* \rightarrow CO$) from the above deposited carbon and lattice oxygen atoms on the TiO_2. As a result, both the MS signals of H_2 and CO can be detected. For the original TiO_2 support [Supplementary Figure 12], barely can any CH_4 be activated in the temperature-programmed process. After Ir deposition, CH_4 cracking occurs, which suggests Ir species are responsible for the CH_4 activation. As shown in Figure 7A and B, the activation of CH_4 over 1.0% Ir/TiO_2 is more inclined to happen than that over 0.05% Ir/TiO_2. The temperature point at which CH_4 starts cracking is in the order of 0.01% (at 380 °C, Supplementary Figure 13) > 0.05 wt% (at 327 °C) > 0.2 wt% (at 270 °C, Supplementary Figure 14) > 0.5 wt% (at 260 °C, Supplementary Figure 15) > 1.0 wt% (at 240 °C). This trend is approximately in line with the above TOF values but still confirms that Ir single atoms are capable of CH_4 activation. Furthermore, CH_4-TPSR experiments were also carried out at 750 ℃ over 0.05% and 1.0% Ir/TiO_2 [Figure 7C and D] to discriminate if there is any difference on the mechanism of CH_4 cracking. To this end, MS signals of C_2H_4 were also additionally monitored because the literature has reported the possibility of C-C coupling to C_2H_4 during the CH_4 cracking process[19,44,54]. Nonetheless, no apparent C_2H_4 signals can be observed in the whole CH_4 cracking process. The above CH_4-TPSR experiments collectively indicate that Ir single atoms have the ability to activate CH_4 and share the same CH_4 decomposition mechanism as that over
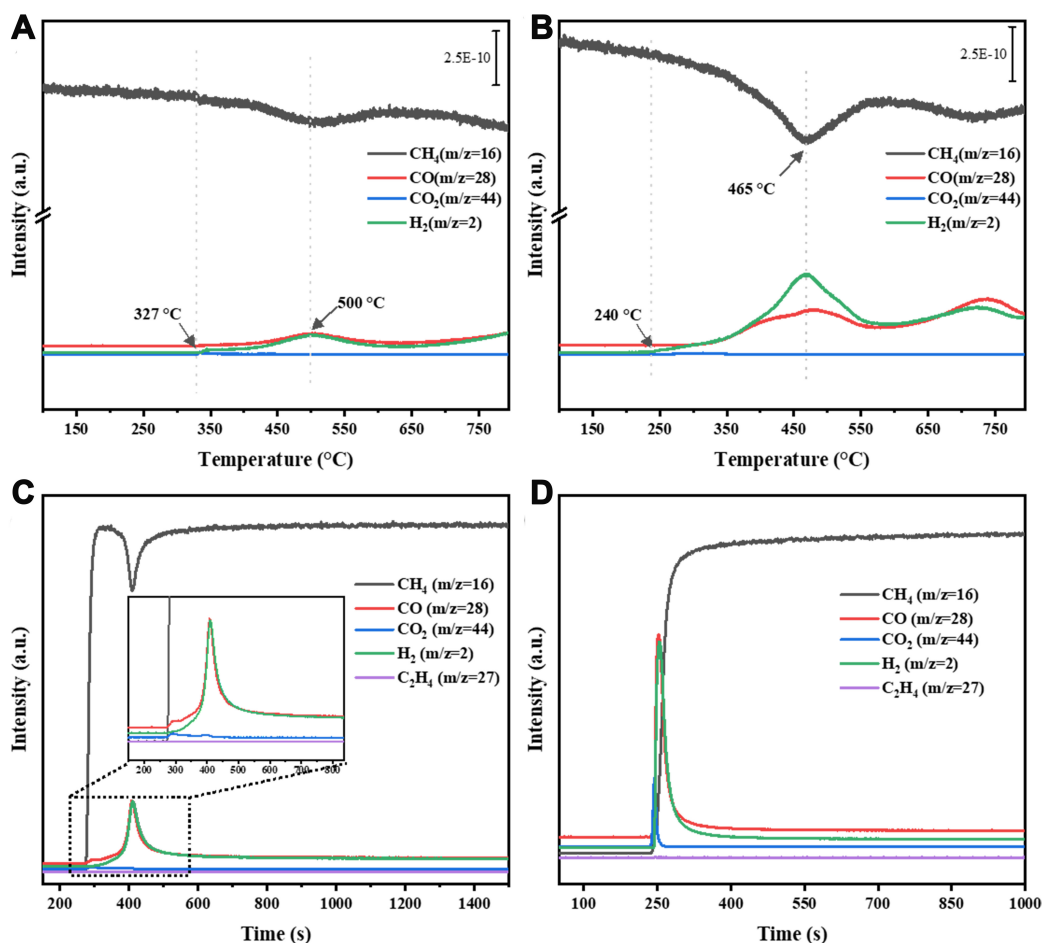
Figure 7. Mass spectrometer signals of CH_4, CO, CO_2, H_2 and C_2H_4 of CH_4-TPSR experiments over (A and B) 0.05% Ir/TiO$_2$, (C and D) 1.0% Ir/TiO$_2$ at elevated temperature and constant 750 °C. TPSR: Temperature-programmed surface reaction.

Ir nanoparticles.

The spent Ir/TiO$_2$ catalysts after DRM reaction for 50 h were then subjected to different characterizations to examine the anti-coking and sintering-resistance properties of Ir species. As shown in Figure 8A, there is nearly no clear weight loss (residual mass above 99.72%) in the high temperature range from 500 to 800 °C by thermal gravimetric analysis (TGA) and the corresponding MS spectra are also absent of the CO_2 (m/z = 44) signals, which manifests nearly no carbon depositions on the Ir/TiO$_2$ catalysts. In addition, in Raman spectra (Figure 8B), the D band at around 1,256 cm^{-1} and G band at around 1,598 cm^{-1} ascribed to sp^3 carbon atoms at defects/disordered sites and sp^2 carbon atoms in graphitic rings, respectively[55,56], cannot be discerned and the strong peaks at 235, 450 and 605 cm^{-1} attributed to rutile TiO$_2$ remain unaffected. Thereupon, Ir/TiO$_2$ catalysts have excellent ability for anti-coking and the harsh reaction conditions have little influence on the TiO$_2$ supports, which can also be confirmed by the XRD patterns of the spent catalysts [Supplementary Figure 16]. Furthermore, the size distributions of Ir species were directly observed by HAADF-STEM. As shown in Figure 9A and B, Ir species of 0.01% and 0.05% Ir/TiO$_2$ catalysts tardily grow to 1.62 and 1.91 nm, which are still smaller than the average size of Ir nanoparticles of around 2-3 nm in the 0.2%, 0.5%, 1.0% Ir/TiO$_2$ ones [Figure 9C-E]. The relatively good sintering resistance of Ir species resulting from the high Tammann temperature meets our experimental anticipations of choosing Ir as active sites for a stable DRM process.
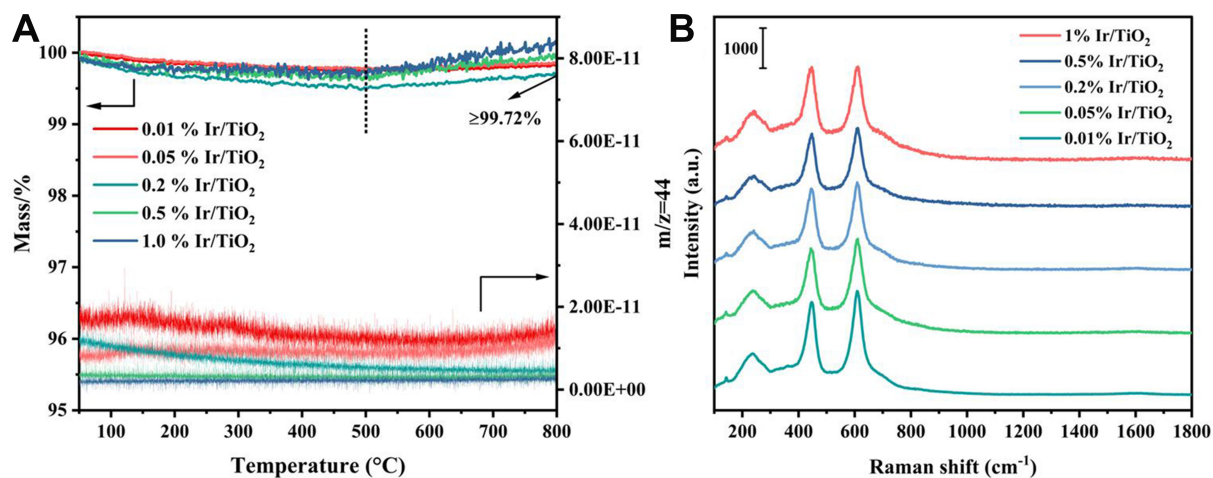
Figure 8. (A) TGA-MS profiles and (B) Raman spectra of spent Ir/TiO_2 catalysts after DRM reaction for 50 h. TGA-MS: Thermogravimetric analysis-mass spectrometry; DRM: dry reforming of methane.
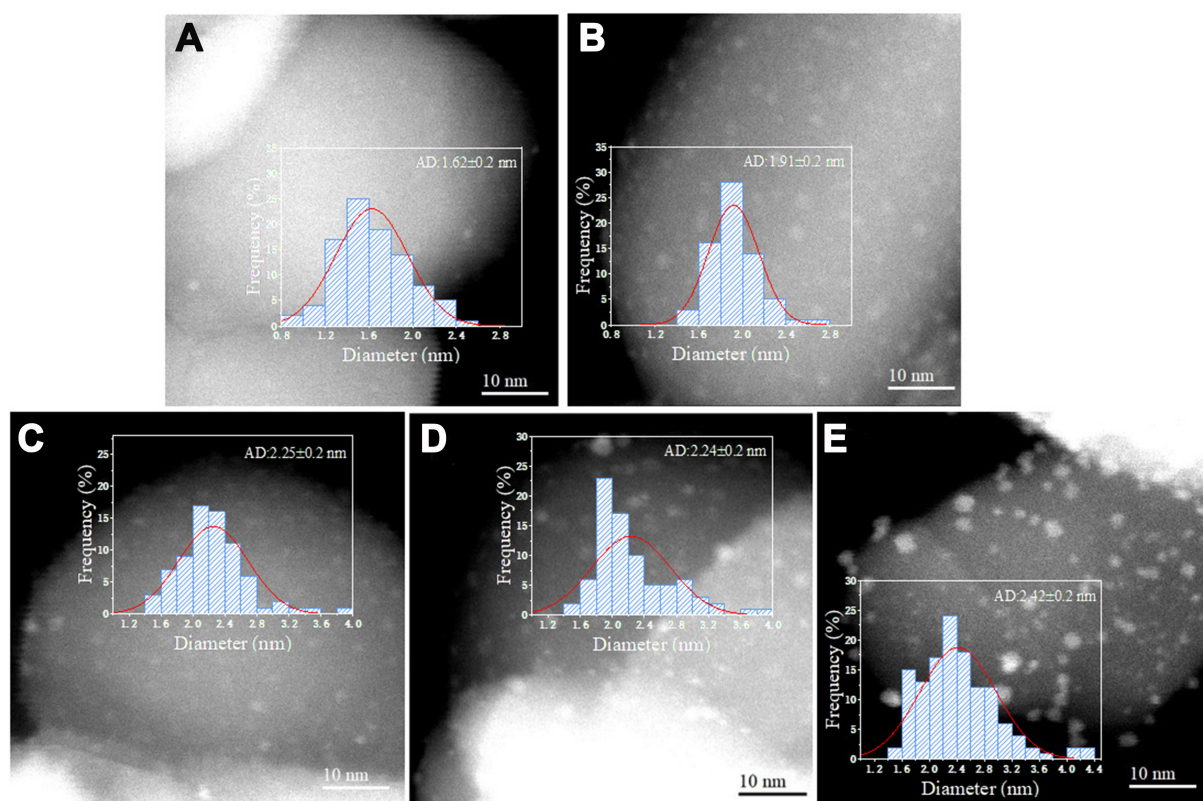

Figure 9. HAADF-STEM images of different Ir/TiO_2 samples after DRM reaction for 50 h. (A) 0.01% Ir/TiO_2; (B) 0.05% Ir/TiO_2; (C) 0.2% Ir/TiO_2; (D) 0.5% Ir/TiO_2; (E) 1.0% Ir/TiO_2. HAADF-STEM: High-angle annular dark-field scanning transmission electron microscopy; DRM: dry reforming of methane.

CONCLUSIONS

In summary, we have synthesized Ir/TiO_2 catalysts via the conventional incipient wetness impregnation method and further downsized the Ir species from a nanoparticulate to a single-atom scale by gradually decreasing Ir loadings. Various characterizations, such as AC-HAADF-STEM, CO-DRIFTs and XAFS,

demonstrated the existence of Ir single atoms on 0.01% and 0.05% Ir/TiO$_2$ samples. In comparison with the DRM performances over the nanoparticulate Ir/TiO$_2$, the Ir SACs show a better specific reaction rate of as high as 697.71 mol$_{CH4}$·g$_{Ir}^{-1}$·h^{-1} at 750 °C, which signifies outstanding Ir atom utilization over Ir single atoms. Besides, the Ir SACs also exhibit excellent stability during the DRM process for 50 h and reveal outstanding anti-coking and good sintering-resistance properties. The strategy of employing Ir single atoms for the maximum atom utilization in the high-temperature reaction process can pave the way for better exploitation of noble metals in other industrial reaction processes.

DECLARATIONS

Authors' contributions
Writing-original draft, visualization, validation, supervision, methodology, investigation, data curation: Li Y
Writing-review and editing, visualization, validation, supervision, methodology, investigation, data curation, conceptualization: Liu C
Investigation, validation: Su Y, Zhao Y
Writing-review and editing, visualization, validation, supervision, resources, investigation, conceptualization: Qiao B

Availability of data and materials
Supplementary Materials is available in the online version of this article.

Conflicts of interest
All authors declared that there are no conflicts of interest.

Ethical approval and consent to participate
Not applicable.

Consent for publication
Not applicable.

Copyright

REFERENCES

1. Han B, Li Q, Jiang X, et al. Switchable tuning CO$_2$ hydrogenation selectivity by encapsulation of the Rh nanoparticles while exposing single atoms. *Small* 2022;18:e2204490. DOI PubMed
2. He D, Wu S, Cao X, et al. Dynamic trap of Ni at elevated temperature for yielding high-efficiency methane dry reforming catalyst. *Appl Catal B Environ Energy* 2024;346:123728. DOI
3. Zhou W, Wang B, Tang L, et al. Photocatalytic dry reforming of methane enhanced by "dual-path" strategy with excellent low-temperature catalytic performance. *Adv Funct Mater* 2023;33:2214068. DOI
4. Xu Y, Yang Y, Wu M, et al. Review on using molybdenum carbides for the thermal catalysis of CO$_2$ hydrogenation to produce high-value-added chemicals and fuels. *Acta Phys Chim Sin* 2024;40:2304003. DOI
5. Kawi S, Kathiraser Y, Ni J, Oemar U, Li Z, Saw ET. Progress in synthesis of highly active and stable nickel-based catalysts for carbon dioxide reforming of methane. *ChemSusChem* 2015;8:3556-75. DOI PubMed
6. Kathiraser Y, Oemar U, Saw ET, Li Z, Kawi S. Kinetic and mechanistic aspects for CO$_2$ reforming of methane over Ni based catalysts. *Chem Eng J* 2015;278:62-78. DOI

7.　Yentekakis IV, Panagiotopoulou P, Artemakis G. A review of recent efforts to promote dry reforming of methane (DRM) to syngas production via bimetallic catalyst formulations. *Appl Catal B Environ* 2021;296:120210. DOI

8.　Wittich K, Krämer M, Bottke N, Schunk SA. Catalytic dry reforming of methane: insights from model systems. *ChemCatChem* 2020;12:2130-47. DOI

9.　Wang Z, Wang M, Huan Y, et al. Defect and interface engineering for promoting electrocatalytic N-integrated CO_2 co-reduction. *Chin J Catal* 2024;57:1-17. DOI

10.　Li T, Chen F, Lang R, et al. Styrene hydroformylation with in situ hydrogen: regioselectivity control by coupling with the low-temperature water-gas shift reaction. *Angew Chem Int Ed Engl* 2020;59:7430-4. DOI PubMed

11.　Chen F, Li T, Pan X, et al. Pd_1/CeO_2 single-atom catalyst for alkoxycarbonylation of aryl iodides. *Sci China Mater* 2020;63:959-64. (in Chinese). DOI

12.　Zhang Y, Yang X, Yang X, et al. Tuning reactivity of Fischer-Tropsch synthesis by regulating TiO_x overlayer over Ru/TiO_2 nanocatalysts. *Nat Commun* 2020;11:3185. DOI PubMed PMC

13.　Rahmati M, Safdari MS, Fletcher TH, Argyle MD, Bartholomew CH. Chemical and thermal sintering of supported metals with emphasis on cobalt catalysts during fischer-tropsch synthesis. *Chem Rev* 2020;120:4455-533. DOI PubMed

14.　Chu W, Wang LN, Chernavskii PA, Khodakov AY. Glow-discharge plasma-assisted design of cobalt catalysts for Fischer-Tropsch synthesis. *Angew Chem Int Ed Engl* 2008;47:5052-5. DOI PubMed

15.　Zhang Q, Akri M, Yang Y, Qiao B. Atomically dispersed metals as potential coke-resistant catalysts for dry reforming of methane. *Cell Rep Phys Sci* 2023;4:101310. DOI

16.　Cheng Q, Yao X, Ou L, et al. Highly efficient and stable methane dry reforming enabled by a single-site cationic Ni catalyst. *J Am Chem Soc* 2023;145:25109-19. DOI PubMed

17.　Zhang X, Xu Y, Liu Y, et al. A novel $Ni-MoC_xO_y$ interfacial catalyst for syngas production via the chemical looping dry reforming of methane. *Chem* 2023;9:102-16. DOI

18.　Feng K, Zhang J, Li Z, et al. Spontaneous regeneration of active sites against catalyst deactivation. *Appl Catal B Environ* 2024;344:123647. DOI

19.　Tang Y, Wei Y, Wang Z, et al. Synergy of single-atom Ni_1 and Ru_1 sites on CeO_2 for dry reforming of CH_4. *J Am Chem Soc* 2019;141:7283-93. DOI PubMed

20.　Carrara C, Múnera J, Lombardo EA, Cornaglia LM. Kinetic and stability studies of Ru/La_2O_3 used in the dry reforming of methane. *Top Catal* 2008;51:98-106. DOI

21.　Niu J, Wang Y, E. Liland S, et al. Unraveling enhanced activity, selectivity, and coke resistance of Pt-Ni bimetallic clusters in dry reforming. *ACS Catal* 2021;11:2398-411. DOI

22.　Al-Fatesh AS, Fakeeha AH, Abasaeed AE. Effect of Pd on CH_4 reforming with CO_2 catalyzed by Ni over mixed Titian-Alumina support. *Adv Mater Res* 2012;476-8:513-8. DOI

23.　Wang D, Littlewood P, Marks TJ, Stair PC, Weitz E. Coking can enhance product yields in the dry reforming of methane. *ACS Catal* 2022;12:8352-62. DOI

24.　Jang WJ, Shim JO, Kim HM, Yoo SY, Roh HS. A review on dry reforming of methane in aspect of catalytic properties. *Catal Today* 2019;324:15-26. DOI

25.　Pakhare D, Spivey J. A review of dry (CO_2) reforming of methane over noble metal catalysts. *Chem Soc Rev* 2014;43:7813-37. DOI

26.　Golunski SE. Final analysis: Why use platinum in catalytic converters? *Platin Met Rev* 2007;51:162. DOI

27.　Li H, Hao C, Tian J, Wang S, Zhao C. Ultra-durable $Ni-Ir/MgAl_2O_4$ catalysts for dry reforming of methane enabled by dynamic balance between carbon deposition and elimination. *Chem Catal* 2022;2:1748-63. DOI

28.　Huang Y, Li X, Zhang Q, Vinokurov VA, Huang W. Enhanced carbon tolerance of hydrotalcite-derived Ni-Ir/Mg(Al)O catalysts in dry reforming of methane under elevated pressures. *Fuel Process Technol* 2022;237:107446. DOI

29.　Zhou R, Sun J, Zhang J, et al. Photo-thermo catalytic dry reforming of methane over $Ni-Ir/SiO_2$ catalyst. *Sci Sin Chim* 2021;51:1539-48. DOI

30.　Nikolaraki E, Goula G, Panagiotopoulou P, et al. Support induced effects on the Ir nanoparticles activity, selectivity and stability performance under CO_2 reforming of methane. *Nanomaterials* 2021;11:2880. DOI PubMed PMC

31.　Kim E, Shin J, Bak J, et al. Stabilizing role of Mo in TiO_2-MoO_x supported Ir catalyst toward oxygen evolution reaction. *Appl Catal B Environ* 2021;280:119433. DOI

32.　Maina SCP, Ballarini AD, Vilella JI, de Miguel SR. Study of the performance and stability in the dry reforming of methane of doped alumina supported iridium catalysts. *Catal Today* 2020;344:129-42. DOI

33.　Jia A, Zhang Y, Song T, et al. The effects of TiO_2 crystal-plane-dependent $Ir-TiO_x$ interactions on the selective hydrogenation of crotonaldehyde over Ir/TiO_2 catalysts. *Chin J Catal* 2021;42:1742-54. DOI

34.　Hou CC, Zou L, Sun L, et al. Single-atom iron catalysts on overhang-eave carbon cages for high-performance oxygen reduction reaction. *Angew Chem Int Ed Engl* 2020;59:7384-9. DOI PubMed

35.　Lang R, Du X, Huang Y, et al. Single-atom catalysts based on the metal-oxide interaction. *Chem Rev* 2020;120:11986-2043. DOI PubMed

36.　Li L, Chang X, Lin X, Zhao ZJ, Gong J. Theoretical insights into single-atom catalysts. *Chem Soc Rev* 2020;49:8156-78. DOI

37.　Wang Y, Su H, He Y, et al. Advanced electrocatalysts with single-metal-atom active sites. *Chem Rev* 2020;120:12217-314. DOI

38.　Kim JH, Shin D, Kim J, et al. Reversible ligand exchange in atomically dispersed catalysts for modulating the activity and selectivity

of the oxygen reduction reaction. *Angew Chem Int Ed Engl* 2021;60:20528-34. DOI

39. Jeong H, Kwon O, Kim B, et al. Highly durable metal ensemble catalysts with full dispersion for automotive applications beyond single-atom catalysts. *Nat Catal* 2020;3:368-75. DOI

40. Zhu R, Kang L, Li L, et al. Photo-thermo catalytic oxidation of C_3H_8 and C_3H_6 over the WO_3-TiO_2 supported Pt single-atom catalyst. *Acta Physico Chimica Sinica* 2024;40:2303003. DOI

41. Zhou Y, Wei F, Qi H, et al. Peripheral-nitrogen effects on the Ru_1 centre for highly efficient propane dehydrogenation. *Nat Catal* 2022;5:1145-56. DOI

42. Han B, Li T, Zhang J, et al. A highly active Rh_1/CeO_2 single-atom catalyst for low-temperature CO oxidation. *Chem Commun* 2020;56:4870-3. DOI PubMed

43. Akri M, El Kasmi A, Batiot-dupeyrat C, Qiao B. Highly active and carbon-resistant nickel single-atom catalysts for methane dry reforming. *Catalysts* 2020;10:630. DOI

44. Akri M, Zhao S, Li X, et al. Atomically dispersed nickel as coke-resistant active sites for methane dry reforming. *Nat Commun* 2019;10:5181. DOI PubMed PMC

45. Yang J, Zhang J, Jiang Q, et al. Highly active and stable Ir nanoclusters derived from Ir_1/$MgAl_2O_4$ single-atom catalysts. *J Chem Phys* 2021;154:131105. DOI

46. Bergeret G, Gallezot P. 3.1.2 Particle size and dispersion measurements. In: Ertl G, Knözinger H, Schüth F, Weitkamp J, editors. Handbook of heterogeneous catalysis. Wiley; 2008. pp. 738-65. DOI

47. Peng M, Dong C, Gao R, Xiao D, Liu H, Ma D. Fully exposed cluster catalyst (FECC): toward rich surface sites and full atom utilization efficiency. *ACS Cent Sci* 2021;7:262-73. DOI PubMed PMC

48. Yang XF, Wang A, Qiao B, Li J, Liu J, Zhang T. Single-atom catalysts: a new frontier in heterogeneous catalysis. *Acc Chem Res* 2013;46:1740-8. DOI PubMed

49. Lu Y, Wang J, Yu L, et al. Identification of the active complex for CO oxidation over single-atom Ir-on-$MgAl_2O_4$ catalysts. *Nat Catal* 2019;2:149-56. DOI

50. Jin R, Peng M, Li A, et al. Low temperature oxidation of ethane to oxygenates by oxygen over iridium-cluster catalysts. *J Am Chem Soc* 2019;141:18921-5. DOI PubMed

51. Zhu Q, Zhou H, Wang L, et al. Enhanced CO_2 utilization in dry reforming of methane achieved through nickel-mediated hydrogen spillover in zeolite crystals. *Nat Catal* 2022;5:1030-7. DOI

52. Zhang Y, Zhang Z, Yang X, et al. Tuning selectivity of CO_2 hydrogenation by modulating the strong metal-support interaction over Ir/TiO_2 catalysts. *Green Chem* 2020;22:6855-61. DOI

53. Wang A, Li J, Zhang T. Heterogeneous single-atom catalysis. *Nat Rev Chem* 2018;2:65-81. DOI

54. Zuo Z, Liu S, Wang Z, et al. Dry reforming of methane on single-site Ni/MgO catalysts: importance of site confinement. *ACS Catal* 2018;8:9821-35. DOI

55. Gangarajula Y, Hong F, Li Q, et al. Operando induced strong metal-support interaction of Rh/CeO_2 catalyst in dry reforming of methane. *Appl Catal B Environ* 2024;343:123503. DOI

56. Zhang Q, Jiang X, Su Y, Zhao Y, Qiao B. Catalytic propane dehydrogenation by anatase supported Ni single-atom catalysts. *Chin J Catal* 2024;57:105-13. DOI